rinds of oceanic basalts (*21*). Fe and S in subseafloor basalts are strongly oxidized in the first 10 million to 20 million years of the basalts' existence (*22*). Oxidation of these chemical species has the potential to support abundant biomass in basaltic aquifers (*22*, *23*). Our results indicate that by 11 Ma and 35 Ma at sites 1225 and 1231, respectively, such oxidation is insufficient to strip dissolved O_2 and NO_3^- from the circulating water, perhaps because the mineral surfaces in contact with water were largely oxidized when the basalt was younger.

19. At each site, the sediment column for which fluxes were calculated spans the interval from 1.5 mbsf to a point midway between the two deepest sample depths. At the open-ocean sites, this interval ends just above the sediment-basalt contact. Given an exponential decline in average cell concentrations with depth (*1*), more than 99% of the total biomass in sediments deeper than 1.5 mbsf lies within our calculational interval at each site.
20. Two moles of C(0) (organic carbon) are oxidized by reducing one mole of SO_4^{2-} to S^{2-}. Five moles of C(0) are oxidized by reducing four moles of NO_3^- to two moles of N_2. Four moles of Fe(III), or two moles of Mn(IV), are required to oxidize one mole of C(0).
21. M. R. Fisk, S. J. Giovannoni, I. H. Thorseth, *Science* **281**, 978 (1998).
22. W. Bach, K. J. Edwards, *Geochim. Cosmochim. Acta* **67**, 3871 (2003).
23. T. Gold, *Proc. Natl. Acad. Sci. U.S.A.* **89**, 6045 (1992).
24. R. A. Jahnke, *Global Biogeochem. Cycles* **10**, 71 (1996).
25. K. B. Sørensen, A. Lauer, A. Teske, *Geobiology*, in press.
26. J. Süß, B. Engelen, H. Cypionka, H. Sass, *FEMS Microbiol. Ecol.*, in press.
27. A. Lauer, A. Teske, *Int. J. Astrobiol.* **3** (S1), 63 (2004).
28. Samples, shipboard facilities, and expedition support were provided by the ODP. The NASA Astrobiology Institute (NAI) supported postcruise analysis of biogeochemical data and precruise development of shipboard biogeochemical techniques. Postcruise culturing studies were supported by grants from the Deutsche Forschungsgemeinschaft. We thank three anonymous reviewers for very helpful comments.

Supporting Online Material
www.sciencemag.org/cgi/content/full/306/5705/2216/DC1
Materials and Methods
References

7 June 2004; accepted 15 October 2004
10.1126/science.1101155

REPORTS

Electron Coherence in a Melting Lead Monolayer

F. Baumberger,* W. Auwärter,† T. Greber, J. Osterwalder‡

We used angle-resolved photoemission spectroscopy to measure the electronic dispersion and single-particle spectral function in a liquid metal. A lead monolayer supported on a copper (111) surface was investigated as the temperature was raised through the melting transition of the film. Electron spectra and momentum distribution maps of the liquid film revealed three key features of the electronic structure of liquids: the persistence of a Fermi surface, the filling of band gaps, and the localization of the wave functions upon melting. Distinct coherence lengths for different sheets of the Fermi surface were found, indicating a strong dependence of the localization lengths on the character of the constituent atomic wave functions.

The transition from the solid to the liquid state can have substantial effects on a material's electronic properties (*1*, *2*). In the case of semiconducting germanium, for example, the forbidden states in the band gap of the crystal are filled and the melt is metallic (*3*, *4*). Understanding the evolution of the electronic wave functions, which underlie such marked changes of the physical properties, represents a prime experimental and theoretical challenge. The main conceptual issue is the lack of any long-range order in liquid or amorphous materials. The periodicity of crystalline solids allows the classification of electronic wave functions as Bloch states (i.e., plane waves, modulated by lattice periodic functions, that extend through the entire crystal). In random systems, such as amorphous solids or liquids, the crystal momentum is no longer a good quantum number and the problem becomes analytically intractable (*1*, *5*, *6*).

Despite decades of intense research, many fundamental problems of the electronic structure of liquids remain unresolved (*7*). In particular, the character of the electronic wave functions (e.g., to what extent they are itinerant or localized) has eluded experimental investigation. The primary experimental problem is the loss of periodicity, which restricts the information provided by the most important experimental probes. A diffraction experiment, which can retrieve the full three-dimensional (3D) atomic structure of a crystalline material, yields only a 1D projection in the form of a pair-correlation length in a liquid or amorphous material (*8*). Analogously, angle-resolved photoemission spectroscopy (ARPES), which gives direct access to the single-particle spectral function $A(k,\omega)$ in crystals, only measures the projection of the momentum-resolved quantity on the energy coordinate (i.e., the spectral density) in a liquid.

Recently, it has been shown in an x-ray diffraction experiment that this limitation can be overcome by working on the interface of a liquid and a crystalline material, which led to the first experimental observation of the fivefold local symmetry (*9*), predicted for monatomic 3D liquids more than 50 years ago (*10*). We use a similar idea to directly measure the electron dispersion and spectral function in a 2D liquid: melted Pb. A crystalline Cu(111) substrate serves as a support with minimal influence on the atomic arrangement of the 2D Pb liquid, and at the same time ensures that the parallel momentum of the initial Pb states is conserved in the photoemission process. In a crystalline environment, the momentum needed for photoemission is supplied in discrete quantities by reciprocal lattice vectors, whereas in a liquid, the photoelectrons gather arbitrary momenta in the process. For a liquid monolayer, however, the momentum of the initial state can be retrieved, because the proximity of the crystalline substrate allows transfer of reciprocal lattice vectors to the liquid states.

Complete momentum distribution maps of the liquid film indicate two Fermi surface sheets, and the spectral function (measured independently for both sheets) reveals novel aspects of the electronic structure of liquids. Contrary to the usual assumptions that accompany the concept of a mobility edge, we find only a negligible energy dependence of the localization length (spatial extension of an exponentially decaying wave function) but a marked momentum dependence. This is interpreted as a manifestation of the different symmetries of the constituent atomic orbitals.

The experiments were performed in a modified VG-ESCALAB 220 spectrometer (*11*) using He Iα radiation (21.22 eV). The energy and angular resolutions were set to 60 meV and ±0.4°, respectively. Pb was evaporated resistively onto a clean Cu(111) surface held

Physikinstitut der Universität Zürich, Winterthurerstrasse 190, CH-8057 Zürich, Switzerland.

*Present address: Department of Applied Physics, Stanford University, Stanford, CA 94305, USA.
†Present address: Department of Physics and Astronomy, University of British Columbia, Vancouver, British Columbia V6T1Z4, Canada.
‡To whom correspondence should be addressed. E-mail: osterwal@physik.unizh.ch

at room temperature (RT) and the coverage was calibrated by x-ray photoelectron spectroscopy and low-energy electron diffraction (LEED) (Fig. 1A). For our ARPES experiments we selected a coverage of 0.8 monolayers (ML), for which we determined a melting temperature T_m of 568 K, in agreement with earlier structural studies (*12*). The melting is demonstrated in the temperature series of LEED patterns, shown in Fig. 1, B to D. Although the six principal Cu(111) diffraction spots remain sharp for all temperatures shown, the Pb-related spots smear out strongly and anisotropically, consistent with the theory of melting for a 2D crystal (*8*, *12*–*15*). Following the analysis of (*12*) for the structure factor along the radial direction close to a Pb(1,0) spot, we obtain the values $\xi(T)$ for the pair-correlation length displayed in Fig. 1F (*16*). For temperatures well above T_m these values drop to about 5 Å, which is of the order of the in-plane lattice constant, signaling the complete melting of the Pb layer.

Before introducing the ARPES results, we briefly describe the electronic states in liquids. In a disordered 2D system, we expect localized electronic states (*1*, *5*). For such states, we can still meaningfully define a momentum as the ensemble average of the momentum expectation value (*1*, *2*). At first glance, we might expect that localized states homogeneously fill momentum space. However, it has been shown that any structure in the atomic pair-correlation length causes maxima in the momentum distribution of the electronic states, and the localized eigenstates of an infinite system are expected to form continuously dispersing bands much like those in a crystalline solid (*1*, *17*). This situation is closely related to that of quasicrystals, where a few dominant points in the densely packed reciprocal lattice, which contribute large values in the Fourier expansion of the ionic potential, cause dispersive peaks in the spectral function. The observation of such dispersive excitations in nonperiodic systems, as recently achieved in quasicrystalline AlNiCo (*18*), is a fundamental task, even though it is clearly not a proof of extended states (*19*). The crucial difference between localized and itinerant states lies in the width of $A(k,\omega)$ at a fixed energy ω_0. This width also relates directly to the transport properties of the liquid (*2*). For a noninteracting solid, $A(k,\omega_0)$ is a sharp delta-function at the energy-momentum position of the electronic band. In the case of a liquid, the spectral function is broadened even without interactions, because a localized eigenstate cannot exhibit a sharp momentum (*2*).

Photoemission Fermi surface maps from the clean substrate and the solid Pb monolayer are shown in Fig. 2, A and B. The Pb-related features—a slightly hexagonal inner Fermi level crossing at $k_{//} \approx 0.6$ Å^{-1} and the small electron pockets at the $\overline{K}$-points (*20*)—are readily identified from a comparison with the density functional calculation for a free-standing planar Pb layer (Fig. 2C) [the intense Shockley surface state on Cu(111) (*21*) is quenched by the adlayer]. The inner part of the electron pockets at $\overline{K}$ is not very distinct in this representation of the data; it can be seen more clearly in the dispersion plot (see below).

The melting transition has a strong impact on the Fermi surface features of the Pb layer (Fig. 3). In these photoemission

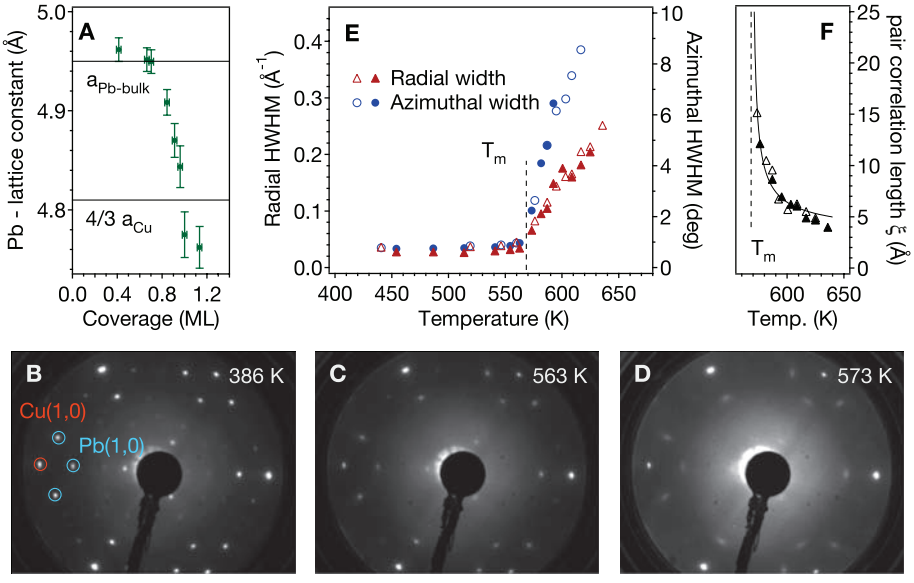

Fig. 1. Structural characterization of the melting transition. (**A**) Coverage dependence of the lattice constant of the first Pb layer on Cu(111). $a_{Pb\text{-}bulk}$ and a_{Cu} denote the respective bulk lattice constants of Pb and Cu. One monolayer (ML) of Pb is defined by the coverage of maximum compression; further Pb must grow in a second layer. (**B** to **D**) LEED patterns of a 0.8-ML film measured with an electron energy of 65 eV at temperatures above and below the melting transition. The Cu(111) principal spots show little temperature dependence, whereas the Pb-related spots smear out strongly. (**E**) Radial (triangles) and azimuthal (circles) half width at half maximum (HWHM) of a Pb(1,0) spot versus temperature. Empty and solid symbols denote measurements for increasing and decreasing temperatures, respectively. (**F**) Radial pair-correlation length ξ, calculated from the radial width of the diffraction spots, assuming a pair correlation function $\propto \exp[-|r|/\xi]$ ($r \to \infty$) (*16*). The solid line is a fit using the critical exponent of 0.37 for a 2D liquid (*14*).

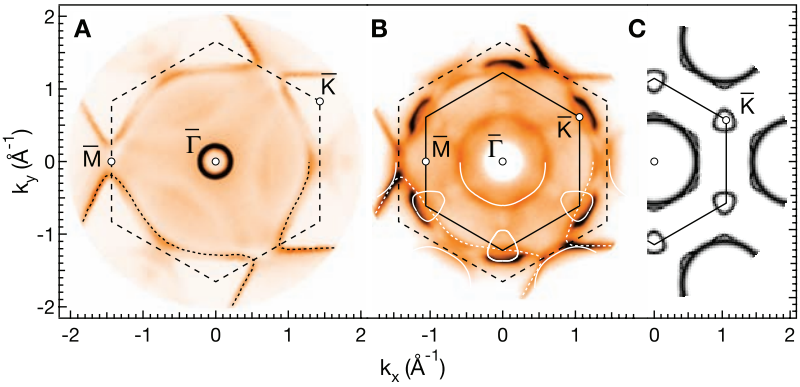

Fig. 2. Fermi surface of the solid Pb monolayer at room temperature. (**A**) Photoemission intensity at the Fermi energy from clean Cu(111), recorded for more than 10^4 emission angles and plotted as a function of the momentum component in the surface plane. The dark (i.e., high-intensity) contours represent sections through the volume Fermi surface of copper, displaying clearly the well-known *L*-point necks (*25*). The dark circle near the center of the plot is due to a free electron–like Shockley surface state (*21*). (**B**) Fermi surface map for the Cu(111) surface covered with 0.8 ML of Pb. The additional contours represent directly the 2D Fermi surface of the incommensurate, hexagonally packed Pb layer. Solid and dashed white lines trace the Pb- and Cu-related features, respectively, and serve as guides to the eye. The Brillouin zones of the incommensurate Cu (dashed) and Pb (solid) surface lattices are plotted in black. (**C**) Density functional theory calculation for a free-standing planar Pb layer, which may serve as a reference to identify the main features of the experimental Fermi surface map.

intensity maps, well-defined Cu contours are observed at all measurement temperatures and serve as a convenient reference for analyzing the Pb states in the liquid layer. Comparison of the Fermi surface in the solid phase at elevated temperature with the RT data in Fig. 2B shows that the dominant features remain unchanged, although the transition widths broaden considerably because of the increased electron-phonon interaction. However, at the melting transition (568 K) the Fermi surface topology changes radically. The electron pockets at the $\overline{K}$-points and the ring-like Fermi contour from the second Brillouin zone coalesce to form one slightly hexagonally modulated ring with $k_{//} \approx 1.4$ Å^{-1} while the inner Fermi surface in the first zone remains visible. Similar to the LEED spots, the Pb-related contours show a gradual smearing out with increasing temperature. The process is not finished at 568 K but proceeds well above T_m, reflecting the continuing decrease of the pair-correlation length. The broadening of the inner Fermi surface is much more severe, indicating a shorter coherence length for states with small momentum.

Before proceeding in the discussion of our results, we address the influence of the crystalline substrate on the spectra from the liquid Pb layer. Fig. 1A shows that the Pb layer grows incommensurate for all coverages—a rather unusual behavior that requires a very weak corrugation of the potential landscape felt by the adatoms. The absence of strong Umklapp features in the Fermi surface map in Fig. 2B indicates a similarly weak lateral coupling of the two electronic systems. Nonetheless, the Pb(1,0) spots in the LEED patterns of Fig. 1, B to D, do not coalesce fully in the azimuthal direction to form a uniform diffraction ring, in agreement with the results of (*12*). The persistence of some azimuthal modulation of the LEED intensities above T_m is likely not a manifestation of the hexatic phase of a 2D liquid (*8*) but reflects the weak (nonzero) corrugation of the substrate potential, which leads to a preferential orientational alignment of the sixfold symmetric elementary building blocks of the 2D liquid. The slight anisotropy of the Fermi surface in the liquid is a direct consequence of this remaining orientational long-range order. However, even in the solid film at elevated temperature, the electronic wave functions are only coherent over a few lattice constants. Therefore, their character can depend only on the short-range correlations, which we expect to be indistinguishable from those in an ideal 2D liquid.

The data in Fig. 4 allow a more detailed look at the electron phase coherence in the liquid film. Raw data showing the dispersion of the electronic states in the solid and liquid phase are shown in Fig. 4, A and B. In the following, we focus on the momentum profile indicated by the solid horizontal line 1.5 eV below the Fermi level, where the different states can be well separated. Three bands are observed: a broad transition from

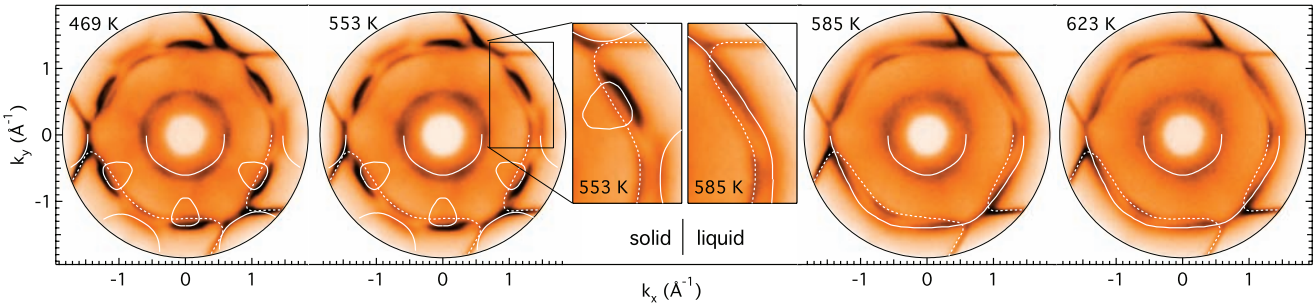

Fig. 3. Evolution of the Fermi surface through the melting transition. Shown are photoemission Fermi surface maps from a 0.8 ML Pb layer on Cu(111), measured at the temperatures indicated in the figure. Melting of the Pb layer occurs between 553 K and 585 K. Note that the copper Fermi surface contours remain sharp throughout the melting transition of the film. The dominant Pb and Cu contours are traced by the solid and dashed white lines, respectively. The inset enlarges the region where the electron pockets around the $\overline{K}$-points and the Fermi surface from the second Brillouin zone of the solid film coalesce to one large Fermi surface in the liquid.

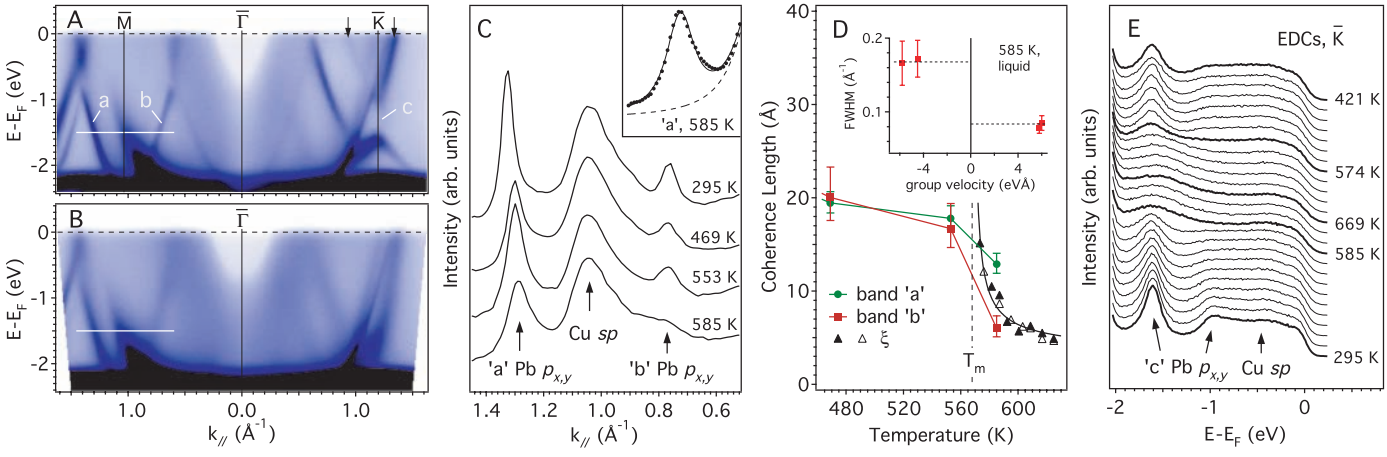

Fig. 4. Electron dispersion and spectral function in the liquid. (**A**) Band dispersion along $\overline{M}$ $\overline{\Gamma}$ $\overline{K}$ for the solid film at RT. The vertical arrows mark the Fermi level crossings of the $\overline{K}$-electron pockets. (**B**) Same as (A) for the liquid film at 585 K. (**C**) Momentum distribution curves at $E - E_F = -1.5$ eV, showing the evolution of the two Pb $p_{x,y}$ bands through the melting transition. The inset shows a Lorentzian spectral function on a smooth background fitted to the transition labeled a in the liquid film. (**D**) Coherence length of the Pb states on the inner and outer Fermi surface as a function of temperature. Error bars reflect the scatter of the results for different functional forms of the background. Also shown is the decay of the radial pair-correlation length in the liquid phase (black symbols, reproduced from Fig. 1F), fitted with the critical exponent for a 2D liquid of 0.37 (*14*). The inset demonstrates the correlation of the momentum broadening with the sign of the group velocity for various points in the band structure. (**E**) EDCs, taken at $\overline{K}$ for various temperatures, demonstrating the reversible filling and opening of a band gap at the melting temperature.

the Cu bulk *sp*-band in the center, framed by two Pb $p_{x,y}$ derived states, dispersing symmetrically around the Brillouin zone boundary of the solid film (*20*). Both Pb bands can clearly be identified in the liquid film, and the inset to Fig. 4C shows that the spectral function of the liquid layer remains to a good approximation Lorentzian (*22*, *23*). However, broadening and decay of intensity upon melting are markedly different for the two states, as is evident in the momentum distribution curves shown in Fig. 4C. The transition labeled b at $k_{//} \approx 0.8$ Å^{-1} washes out almost completely, whereas the peak a at 1.3 Å^{-1} is much less affected by the melting. Fig. 4D summarizes the behavior of $A(k,\omega_0)$ for different points in the band structure of liquid Pb. For all states, we find a clear momentum broadening at the melting transition (*24*). However, for states belonging to the outer Fermi surface, the broadening is only modest. These states therefore essentially conserve their character through the phase transition. Contrarily, states on the small Fermi surface change qualitatively from extended states in the solid film to highly localized states in the liquid. It is illustrative to convert wave numbers and peak widths for the transitions a and b to wavelengths $\lambda = 2\pi/k$ and radial coherence lengths Δk^{-1} of the photo hole wave functions. We find $\lambda = 4.8$ Å and $\Delta k^{-1} \geq 12$ Å for state a, versus $\lambda = 7.9$ Å and $\Delta k^{-1} \approx 4$ Å for state b. The latter state with longer wavelength thus exhibits supercritical damping and does not fulfill the basic condition for extended states: It may be considered fully localized (*1*). The same analysis has been carried out over the entire accessible energy range (–1.9 eV to E_F), and no marked change of the coherence length with energy was found.

A striking indication for loss of coherence can be observed at the nominal Brillouin zone boundary where the $\overline{K}$-gap around 1.5 eV binding energy disappears upon melting (feature c in Fig. 4, A and B). A set of energy distribution curves (EDCs) taken at $\overline{K}$ for various temperatures is shown in Fig. 4E. Clearly, the melting temperature represents a sharp break where the spectra change qualitatively: The two Pb-related peaks from below and above the band gap disappear, and a new very broad structure emerges close to the lower band edge. The momentum distribution of the liquid states that evolve in the band gap of the solid film is comparable to the states on the inner Fermi surface, indicating a high localization, consistent with basic models (*1*, *7*). Figure 4E also shows that the melting transition is fully reversible.

We propose that the key to the different behavior of states on the inner and outer Fermi surfaces lies in the character of the atomic wave functions that constitute the bands. Both wavelength and symmetry of the wave functions may be important. Intuitively, one might expect a higher susceptibility to disorder for states with a short wavelength (*17*), but this is opposite to the trend observed in the data. Thus, the key effect appears to be the symmetry of the constituent atomic wave functions. The band that forms the small Fermi surface exhibits a negative group velocity; that is, the band energy decreases with increasing wave vector. This is characteristic of *p*-type wave functions that change their phase at the nucleus site. In a tight-binding picture, the band minimum lies at the Brillouin zone boundary where neighboring atoms contribute to the overall wave function with opposite phases, thus maximizing the mutual overlap. In the liquid state the zone boundary no longer exists, and these states thus lose their phase reference. Bands with positive group velocity, such as those that form the outer Fermi surface in the liquid, are of even symmetry and refer their phases to the Γ point, which persists in the liquid state to serve as a phase anchor.

References and Notes

1. N. F. Mott, *Adv. Phys.* **16**, 49 (1967).
2. L. E. Ballentine, *Adv. Chem. Phys.* **31**, 263 (1975).
3. G. Kresse, J. Hafner, *Phys. Rev. B* **49**, 14251 (1994).
4. P. Oelhafen, M. G. Garnier, *J. Electron Spectrosc.* **124**, 211 (2002).
5. P. W. Anderson, *Phys. Rev.* **109**, 1492 (1958).
6. J. Hafner, M. Krajci, in *Physical Properties of Quasicrystals*, Z. M. Stadnik, Ed. (Springer, Berlin, 1999), pp. 209–256.
7. P. A. Lee, T. V. Ramakrishnan, *Rev. Mod. Phys.* **57**, 2287 (1985).
8. R. J. Birgeneau, P. M. Horn, *Science* **232**, 329 (1986).
9. H. Reichert *et al.*, *Nature* **408**, 839 (2000).
10. F. C. Frank, *Proc. R. Soc. London Ser. A* **215**, 43 (1952).
11. T. Greber *et al.*, *Rev. Sci. Instrum.* **68**, 4549 (1997).
12. B. H. Müller, Th. Schmidt, M. Henzler, *Surf. Sci.* **376**, 123 (1997).
13. J. M. Kosterlitz, D. J. Thouless, *J. Phys. C* **6**, 1181 (1973).
14. D. R. Nelson, B. J. Halperin, *Phys. Rev. B* **19**, 2457 (1979).
15. A. P. Young, *Phys. Rev. B* **19**, 1855 (1979).
16. In the vicinity of a diffraction spot, the structure factor takes the form $S(\mathbf{K}) \propto [1 + \xi^2 |\mathbf{K} - \mathbf{G}|^2]^{-3/2}$ for an asymptotic radial pair-correlation function $\propto \exp[-|r|/\xi]$ ($r \rightarrow \infty$), where **K** is the scattering vector, **G** is the reciprocal lattice vector associated with the particular LEED spot, and ξ is the temperature-dependent pair-correlation function.
17. S. F. Edwards, *Philos. Mag.* **6**, 617 (1961).
18. E. Rotenberg, W. Theis, K. Horn, P. Gilles, *Nature* **406**, 602 (2000).
19. F. Baumberger *et al.*, *Phys. Rev. Lett.* **92**, 196805 (2004).
20. F. Baumberger, A. Tamai, M. Muntwiler, T. Greber, J. Osterwalder, *Surf. Sci.* **532–535**, 82 (2003).
21. F. Reinert, G. Nicolay, S. Schmidt, D. Ehm, S. Hüfner, *Phys. Rev. B* **63**, 115415 (2001).
22. Numerical simulations for other liquid metals show rich structure in the spectral function (*23*). Currently, we cannot discern this structure in the low signal, but our data do not exclude non-Lorentzian line shapes.
23. S. K. Bose, O. Jepsen, O. K. Andersen, *Phys. Rev. B* **48**, 4265 (1993).
24. Momentum distribution curves have been fitted with a convolution of a Lorentzian and a Gaussian of 0.03 Å^{-1} full width at half maximum, which accounts approximately for the combined energy and momentum resolution.
25. P. Aebi, J. Osterwalder, R. Fasel, D. Naumovic, L. Schlapbach, *Surf. Sci.* **307–309**, 917 (1994).

26. We thank A. Seitsonen, J. Hutter, P. Zeppenfeld, K. M. Shen, N. J. C. Ingle, and Z.-X. Shen for fruitful discussions. Supported by the Swiss National Science Foundation.

12 August 2004; accepted 4 November 2004
Published online 25 November 2004;
10.1126/science.1103984
Include this information when citing this paper.

Detection of a Deep 3-μm Absorption Feature in the Spectrum of Amalthea (JV)

Naruhisa Takato,[1]* Schelte J. Bus,[2] Hiroshi Terada,[1] Tae-Soo Pyo,[1] Naoto Kobayashi[3]

Near-infrared spectra of Jupiter's small inner satellites Amalthea and Thebe are similar to those of D-type asteroids in the 0.8- to 2.5-micrometer wavelength range. A deep absorption feature is detected at 3 micrometers in the spectra of the trailing side of Amalthea, which is similar to that of the non-ice components of Callisto and can be attributed to hydrous minerals. These surface materials cannot be explained if the satellite formed at its present orbit by accreting from a circumjovian nebula. Amalthea and Thebe may be the remnants of Jupiter's inflowing building blocks that formed in the outer part or outside of the circumjovian nebula.

The jovian system has three classes of satellites: outer small satellites, large regulars (Galilean satellites), and inner small regulars. The outer small satellites were probably products of early capture from heliocentric orbits (*1*, *2*), and the Galilean satellites formed by circumjovian accretion (*1*, *3*), but the origin of the inner small satellites is still uncertain (*4*). There are four small satellites inside Io's orbit. Amalthea and Thebe are the outer two satellites among these, revolving at 2.54 and 3.11 Jupiter radii, respectively. The size of Amalthea is 270 by 165 by 150 km and that of Thebe is 116 by 98 by 84 km (*5*, *6*). Almathea and Thebe may have formed by accretion from the circumjovian nebula (*1*, *7*) because they have low-inclination ($i = 0.39°$ and 1.07°, respectively) and low-eccentricity ($e = 0.003$ and